Journal of Materials Chemistry A

Accepted Manuscript

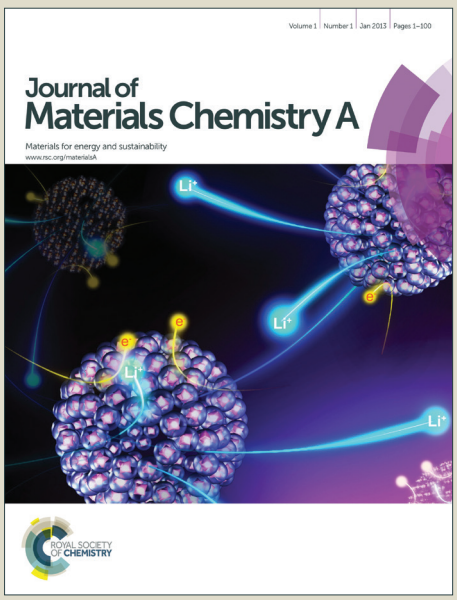

ROYAL SOCIETY OF CHEMISTRY

www.rsc.org/materialsA

Journal Name

RSCPublishing

ARTICLE

Effect of La-Doping on Optical Bandgap and Photoelectrochemical Performance of Hematite Nanostructures

Cite this: DOI: 10.1039/xoxxoooooox

Ning Li[a,b], Sundaramurthy Jayaraman[b,c], Si Yin Tee[a,d], Palaniswamy Suresh Kumar[b,c], Coryl Jing Jun Lee[a], Siao Li Liew[a], Dongzhi Chi[a], T. S. Andy Hor[a,e], Seeram Ramakrishna[b*], He-Kuan Luo[a**]

Received ooth January 2012,
Accepted ooth January 2012

DOI: 10.1039/xoxxoooooox

www.rsc.org/

La-doped hematite nanotubes are fabricated by electrospinning of a sol-gel solution consisting of La(III) acetylacetonate hydrate/polyvinylpyrrolidone(PVP)/ferric acetylacetonate, and subsequent sintering at 500 °C for 5 h in air. Further grinding of these nanotubes affords the La-doped hematite nanoparticles. FESEM EDX indicates the La content is 3.66 mol% in the La-doped hematite. HRTEM and XRD reveal that La^{3+} cations are doped into the hematite crystal lattice. UV-Vis diffuse reflectance shows better light absorption for La-doped hematite, with bandgap reduced from 2.58 eV to 2.46 eV. EIS and four-probe characterization demonstrate the La-doping reduces charge transfer resistance and increases the electrical conductivity, thus leads to improved charge transportation. Photoelectrochemical (PEC) water splitting studies show that La-doped hematite nanoparticles demonstrate net photocurrent density up to 0.112 and 0.270 mA/cm^2 at 1.23 and 1.60 V *vs* RHE under 100 mW/cm^2 simulated solar irradiation, which are 187% and 63% higher than pristine hematite nanoparticles respectively. The effect of La-doping on improving electrical conductivity, light absorption and PEC performance is mainly attributed to the intensification of crystal orientation along (110) plane and the lattice expansion caused by the La^{3+} cations which have much bigger radius and are more electron-rich than Fe^{3+}.

Introduction

In the past few decades, metal oxides have opened up a new era in developing advanced functional materials and exploring their diversified applications.[1-4] Dated back to 1972, Honda and Fujishima[5] carried out the pioneering research of using TiO_2 as electrode for photoelectrochemical (PEC) water splitting. Ever since then, water splitting by semiconducting metal oxides,[6,7] sulfides,[8,9] carbon nitrides,[10] molecular devices,[11,12] etc., has emerged as a promising strategy for solar energy harvest and storage. Among all the semiconducting metal oxides, hematite (α-Fe_2O_3) attracts much scientific attention by virtue of its favourable bandgap width and high energy conversion efficiency with a theoretical value of 16.8%.[13,14] Its excellent chemical stability, non-toxicity, abundance and cost-effectiveness further make hematite a very much suitable photoelectrode material. But all these favourable characteristics are balanced against its low electrical conductivity, short hole diffusion length, limited light absorption efficiency, and poor oxygen evolution kinetics.[15-18]

To improve the PEC performance, two strategies have been reported to modify the hematite semiconductor. The first one is doping various heteroatoms into the hematite crystal lattice, such as Zr, Si, Sn, Ti, Al, Mg, Zn, I, Mo and Cr.[15,19-26] All of these dopants are able to enhance the PEC performance at different degrees via different mechanisms. For example, Zn is transformed into wide band gap ZnO and hence facilitates the charge carrier migration.[24] Whereas Si dopant acts as electron donor due to the substitution of Fe^{3+} by Si^{4+} in the hematite crystal lattice and thereby improves the electrical conductivity.[19] The second strategy is to fabricate hematite nanostructures. In principle, reducing the hematite feature size down to nanometer scale significantly enlarges the photoelectrode/electrolyte interface affording more catalytically active sites. The diffusion path of minority carriers for collecting more photogenerated charges is greatly reduced as well. Many synthetic techniques, such as solution-based colloidal approach, ultrasonic spray pyrolysis, hydrothermal, atmospheric pressure chemical vapor deposition and template-based methods, have been reported for fabricating various hematite nanostructures with high effectiveness and low cost.[27-31] We herein report an alternative strategy, i.e. electrospinning, to fabricate La-doped hematite nanotubes and nanoparticles.

As a facile and versatile technique for nanomaterial fabrication, electrospinning has attracted enormous attention in diversified research fields.[32,33] The electrospun nanofibers generally have a diameter ranging from tens to hundreds of

nanometers with a fiber length up to several centimeters. This synthetic approach has demonstrated a wide range of applications in electronics, healthcare, energy, biotechnology, etc.[33]

Rare earth metals have bigger atomic radius and more electron-rich in outer shell compared to 3d metals, such as Fe and Ti. It is reported that doping rare earth metals can improve the chemical and electrochemical properties of metal oxides.[34-38] For example, the La-cation in perovskite type semiconductor with ABO_3 format, such as $SrTiO_3$, is able to substitute the A site cations and slow down the charge carrier recombination.[37] But doping rare earth metals into hematite received little attention in developing new photocatalysts for water splitting. Recently, Labhsetwar and co-workers[38] reported the fabrication of perovskite type $LaFeO_3$ nanoparticles, and investigated its photocatalytic performance for water splitting using ethanol as sacrificial agent under visible light. Liu and co-workers[39] reported another strategy of depositing upconversion rare-earth nanocrystals of $NaYF_4$:Yb,Er, which is able to assist hematite substrate to harness infrared radiation. To the best of our knowledge, La-doped hematite nanotubes and nanoparticles have not been fabricated and studied for PEC water splitting. Therefore, herein we present our fabrication of one dimensional (1D) La-doped hematite nanotubes via electrospinning and sintering, followed by a facial grinding into nanoparticles. These nanotubes and nanoparticles are characterized with FESEM, TEM and XRD. The effect of La-doping on charge transfer resistance, electrical conductivity, light absorption and PEC performance is investigated. EIS and four-probe characterization show that the La-doping leads to reduced charge transfer resistance and improved electrical conductivity. UV-Vis diffuse reflectance reveals improved light absorption for La-doped hematite. PEC water splitting studies further demonstrate that the La-doped hematite nanostructures display higher photocurrent density relative to pristine hematite.

Experimental Sections

Materials

Polyvinylpyrrolidone (PVP, average MW=1,300,000), polyethylene oxide (PEO, average MW=100,000), ferric acetylacetonate ($Fe(acac)_3$) 97%, and La (III) acetylacetonate hydrate ($La(acac)_3{\bullet}xH_2O$) (27.3 ~ 31.2 % La, complexiometric EDTA)were purchased from Sigma-Aldrich, Singapore. Glacial acetic acid (≥ 99% purity) and absolute ethanol (≥ 99% purity) were purchased from Tedia, Singapore. All chemicals were used as received without any further purification. High purity water (resistivity >18 MΩ) was used throughout the experiment. Fluorine-doped tin oxide (FTO) was purchased from Solaronix and ultrasonicated in ethanol and water for 30 min each prior to use.

Nanostructure Fabrication

1.0 g PVP was added to 10 mL absolute ethanol and magnetically stirred at room temperature. Upon complete dissolving, 400 mg $Fe(acac)_3$, 60mg $La(acac)_3{\bullet}xH_2O$ and 1.0 mL glacial acetic acid were added in the PVP solution followed by another 12 h stirring. The obtained dark-red solution was then put for electrospinning with 22G½ pinhead syringe and 18.5 kV applied voltage (Electrospunra, Mikrotools Pte. Ltd., Singapore). Distance between the pinhead and the aluminum foil collector was 15 cm, and precursor flow rate was 1.0 mL/h. Humidity in the electrospinning chamber was kept at 40%. The obtained composite fibers were then stored in a desiccator for about 6 h at room temperature before annealing at 500 °C for 5 h in air. La-doped hematite nanoparticles were prepared by grinding the nanotubes in mortar for around 1 minute. For comparison, the pristine hematite nanofibers and nanoparticles were fabricated using identical procedures without $La(acac)_3{\bullet}xH_2O$ addition. The electrospinning voltage needs to be adjusted accordingly.

Nanomaterial Characterization

Material crystallinity was characterized using powder X-ray diffraction (XRD) (Shimadzu XRD-6000, Cu Kα radiation operating at 30 kV / 40 mA). Field emission scanning electron microscopy (FESEM) images and Energy-dispersive X-ray (EDX) spectrum were obtained using a JEOL JSM 6700F with an Oxford ISIS x-ray EDS microanalysis system. TEM analysis was carried out using JOEL JEM 2100 with operation voltage of 200 kV. UV-Vis diffuse reflectance was recorded using UV3600, UV-Vis-NIR Spectrophotometer, SHIMADZU. Thermal decomposition behaviour of the electrospun composite fibers was characterized in N_2 atmosphere using simultaneous thermal analyser, STA 449F1, NETZSCH. Material surface area and porosity distribution were obtained from N_2 adsorption/desorption isotherms at 77 K (Micrometrics ASAP 2020). Electrochemical impedance spectroscopy (EIS) analysis was carried out using Metrohm Autolab Potentiostats (Model PGSTAT 128N) with hematite working electrode, Pt counter electrode and Ag/AgCl (3M KCl) (Metrohm, Switzerland) reference in 1 M KOH electrolyte. The potential was set 0.23 V vs Ag/AgCl with 10,000 Hz~0.1 Hz frequency range. Electrical conductivity was measured using the four-probe system from MICRO XACT, INC. Simulated light source (Hamamatsu, Lightningcure™) was used with spectrum ranging from 300 nm to 700 nm at intensity of 100 mW/cm^2, calibrated using Si-based solar intensity detector.

PEC Water Splitting Measurement

La-doped hematite photoelectrode was fabricated using doctor-blading technique. The prepared devices were sintered at 500 °C for 1 h in air to remove the PEO binder. PEC water splitting performance of the prepared photoelectrode was measured using the same PEC setup and light source with EIS analysis. The device fabrication and measurement procedures were kept identical for pristine hematite nanomaterials unless otherwise stated.

Results and Discussions

Crystallinity and Morphology Studies

The electrospun $La(acac)_3{\bullet}xH_2O/Fe(acac)_3$/PVP composite fibers display a clear web-like configuration (see Fig. 1**a**) instead of the conventional fiber structures obtained without $La(acac)_3{\bullet}xH_2O$ (Fig. 2**a**). This morphology change can be explained by the presence of water molecules in the La precursor. Water molecules are able to form hydrogen bonding with ethanol and lead to incomplete solvent evaporation during electrospinning jet travelling. Thus the wet fibers easily merge with each other at the crossing points after reaching the collector. The fiber joints are smooth and continuous with no slits or cracks, as shown in the inset of Fig. 1**a**. After sintering at 500 °C for 5 h, the web-like composite fibers turn into

disconnected nanotubes (Fig. 1**b**). During the sintering process, material morphology is determined by two opposite mechanisms.[40] One is the diffusion of gases generated from the residual solvent evaporation and precursor decomposition , which contributes to fiber swelling and hollow structure formation.[40] The other mechanism is fiber shrinkage driven by the precursor coalescing, which facilitates the development of particle-embedded solid nanofibers.[41] It is very likely that the hollow nanotubes of La-doped hematite are formed due to the dominance of gas diffusing effect. In the composite fibers containing $La(acac)_3 \bullet xH_2O$, the additional water molecules and acetylacetonate molecules contribute to a stronger gas diffusing effect, which oversteps the shrinkage mechanism, thus affords the nanotube structure. However, in the absence of $La(acac)_3 \bullet xH_2O$, the obtained $Fe(acac)_3$/PVP composite fiber has less gas diffusion, which is not able to counterbalance the fiber shrinkage. Therefore, the hematite nanofibers are formed (Fig. 2**b**). The formation mechanism needs further studies, as it is a complex process determined by both the material composition and sintering procedures.[40] The La-doped nanotubes have inner and outer diameters of (113±24) and (177±38) nm, respectively, contributing to a larger surface area compared to the pristine hematite nanofibers that have a relatively smaller diameter of (135±22) nm.

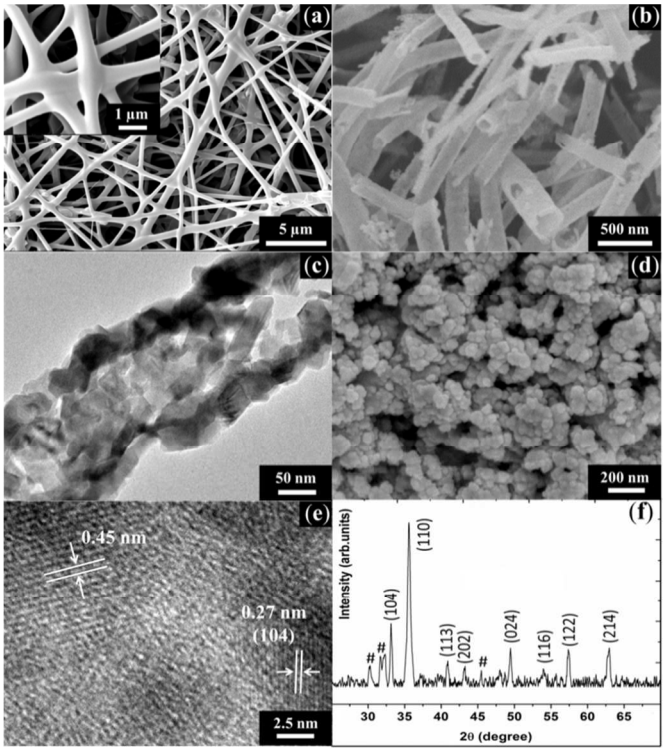

Fig. 1 FESEM images: (a) Electrospun composite fibers containing $La(acac)_3/Fe(acac)_3$/PVP, inset is the fiber joint; (b) La-doped hematite nanotubes after sintering. (c) TEM image of La-doped hematite nanotubes. (d) FESEM image of La-doped hematite nanoparticles. (e) HRTEM of La-doped hematite with the lattice planes displayed. (f) XRD pattern of La-doped hematite nanotubes. Miller indices are shown, and peaks are well indexed to hematite (JCPDS: 33-0664). # symbol indicates peaks due to the γ-Fe_2O_3 and Fe_3O_4 impurities.

The TEM images of Fig. 1**c** and Fig. 2**c** further reveals that both the nanotubes and nanofibers are formed by self-assembling of nanoparticles. Therefore, they can be easily grinded into the corresponding nanoparticles (see Fig. 1**d** and Fig. 2**d**). The HRTEM image (Fig. 1**e**) depicts inter-planer space of 0.27 nm, which correlates to the hematite lattice plane (104). A greater lattice spacing of 0.45 nm is also observed, but it does not correspond to any plane of hematite crystal lattice. This greater lattice spacing may be due to La-doping because the radius of La^{3+} (1.18 Å) is much larger than Fe^{3+} (0.55Å),[42] requiring more space to accommodate the La^{3+} cations in the hematite crystal.

The sharp XRD peaks of both La-doped hematite and pristine hematite (see Fig. 1**f** and Fig. 2**f**) clearly reveals the high quality crystalline nature of the obtained materials. Despite some γ-Fe_2O_3 and Fe_3O_4 impurities, all the peaks can be well indexed to hematite (JCPDS: 33-0664, a = 5.035 Å, c = 13.749 Å). But for La-doped hematite, shifting of the (110) and (024) peaks is observed (see Fig. 3). The shifting is towards lower 2θ value, indicating an increase of lattice parameter.[42] This is in good agreement with the enlarged lattice spacing of 0.45 nm observed in HRTEM (see Fig. 1**e**). La-doped hematite also demonstrates slightly higher XRD noise level than pristine hematite, probably due to the smaller grain size in La-doped hematite. The difficult substitution of Fe^{3+} by La^{3+} may result in certain amount of La species existing as highly dispersed crystallite, which retards the formation of large hematite crystal grains.[42]

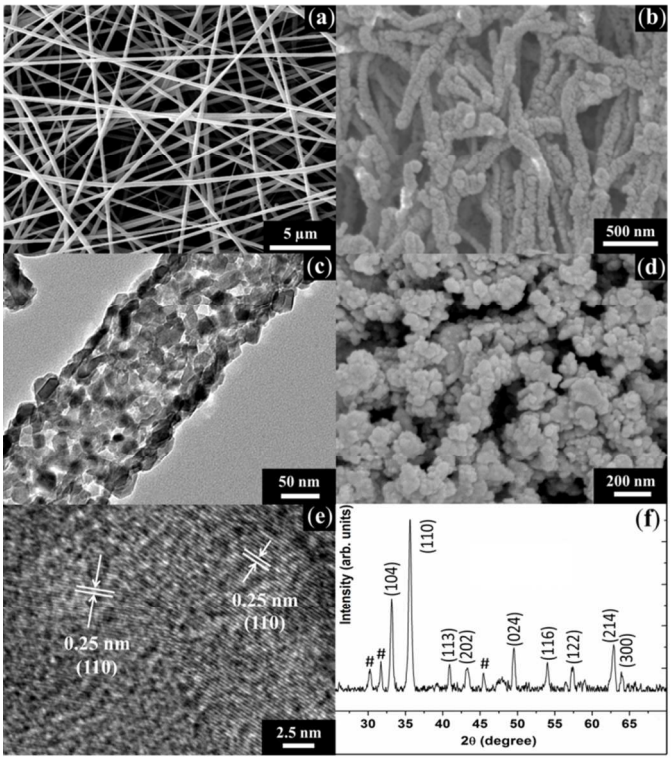

Fig. 2 FESEM images: (a) Electrospun $Fe(acac)_3$/PVP composite fibers; (b) Pristine hematite nanofibers after sintering. (c) TEM image of pristine hematite nanofibers. (d) FESEM image of pristine hematite nanoparticles. (e) HRTEM lattice image of pristine hematite with the shown lattice spacing corresponding to (110) plane. (f) XRD pattern of pristine hematite nanofibers. Miller indices are shown. # symbol indicates peaks due to the γ-Fe_2O_3 and Fe_3O_4 impurities.

In the XRD pattern of La-doped hematite, we have to take a special note that the (110) peak is intensified compared to its pristine counterpart. In Fig. 1**f**, the ratio of integrative peak areas between (110) and (104) peaks is 4.53, that is more

significant than the ratio of 2.16 between peaks (110) and (104) in Fig. 2**f**. This clearly indicates that La-doping significantly contributes to preferential (110) crystal orientation parallel to the substrate, which corresponds to (001) basal plane normal to the substrate. In view of hematite conductivity anisotropy, the electrical conductivity along the (001) plane is about four orders of magnitude higher than its perpendicular planes.[43,44] Therefore, a much higher electrical conductivity is expected for La-doped hematite, which is proved by four-probe electrical conductivity characterization. In general, a higher electrical conductivity is favorable for PEC water splitting because the photogenerated charge carriers can reach their reactive sites more effectively to participate in water oxidation and reduction. This is also proved by PEC water splitting studies that La-doped hematite nanoparticles display much higher photocurrent density compared to the pristine hematite nanoparticles.

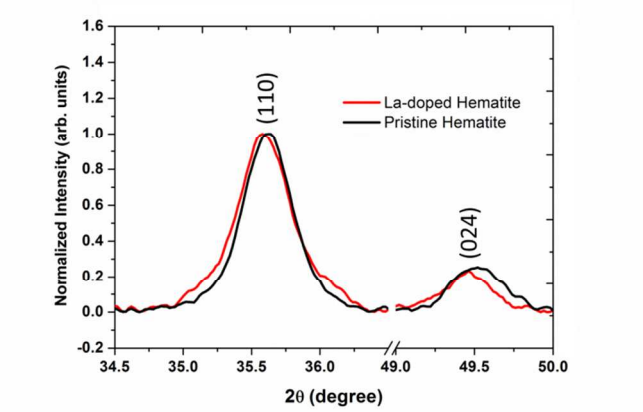

Fig. 3 Comparison of XRD patterns showing peak shift after La-doping inside hematite crystal lattice

UV-Vis Reflectance, TGA, BET and FESEM EDX Analysis

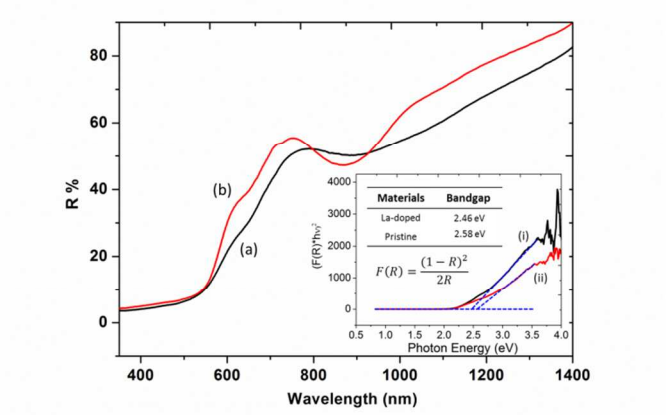

Fig. 4 Diffuse Reflection spectra of powder-form (a) La-doped hematite nanotubes and (b) pristine hematite nanofibers. Inset is corresponding plot of Kubelka-Munk function versus the incident photon energy. Curve (i) is for La-doped hematite and curve (ii) is for pristine hematite.

The diffuse reflection spectra (with zero transmission) are recorded as shown in Fig. 4. It can be clearly observed that the absorption edge of La-doped hematite (curve **a**) is shifted to longer wavelength relative to pristine hematite (curve **b**), suggesting a reduced bandgap in the La-doped hematite materials. Also, the diffuse reflection from La-doped hematite is lower than that from pristine hematite in the entire wavelength window except for the 790~936 nm region. In the 300~530 nm region, reflection values are low and the difference is minimal, indicating good absorption for both materials. Whereas in the long wavelength visible (530~790 nm) and infrared (>936 nm) regions, La-doped hematite displays notably lower reflection, evincing a better absorption of photons in both regions. Their corresponding bandgaps are calculated from the modified Kubelka–Munk function, as shown in inset of Fig. 4. La-doped hematite possesses a relatively smaller bandgap (2.46 eV) compared to its pristine counterpart (2.58 eV), which is in good agreement with its lower reflection values shown in Fig. 4.

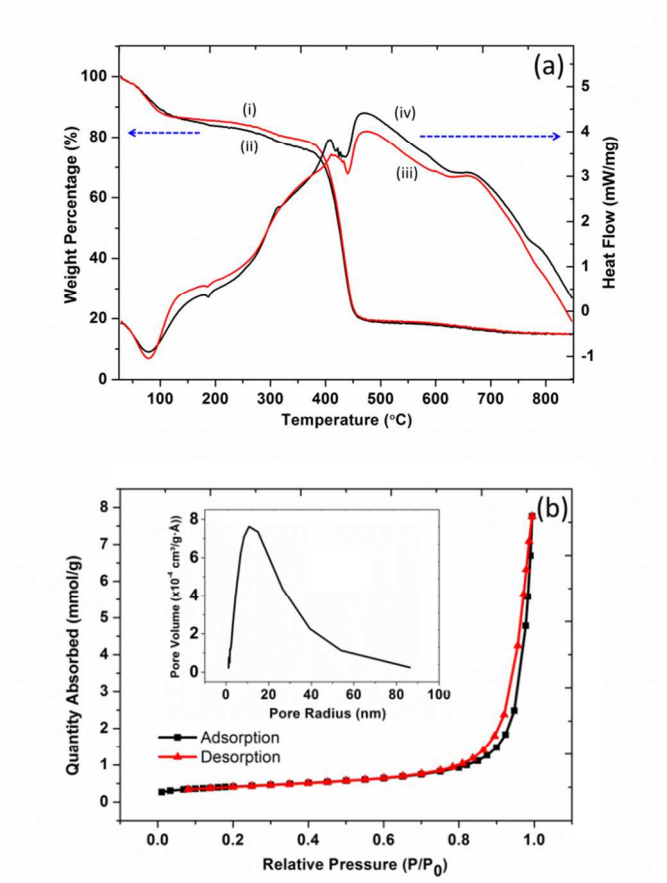

Fig. 5 (a) TGA and DSC analysis of electrospun composite fibers; (i) and (iii) are for $La(acac)_3/Fe(acac)_3$/PVP composite fibers; (ii) and (iv) are for $Fe(acac)_3$/PVP composite fibers. (b) N_2 adsorption-desorption isotherm for La-doped hematite nanotubes; inset is the BJH pore size distribution.

Thermogravimetric analysis (TGA) is carried out to study the weight loss behaviour of $La(acac)_3/Fe(acac)_3$/PVP and $Fe(acac)_3$/PVP composites fibers. Both of them show an overall weight loss of about 85% after sintered at an elevated temperature up to 800 °C (see Fig. 5**a**). The weight loss occurring below 100 °C is attributed to the evaporation of residual solvent in the composite fibers. Further weight loss above 150 °C is due to the partial decomposition of the acetylacetonate molecules. The conversion from $Fe(acac)_3$ to hematite occurs in the temperature range of 230 °C ~ 365 °C.[45] In this range, curve **i** with $La(acac)_3$ is slightly higher than **ii** without $La(acac)_3$, possibly due to the additional weight loss of the La-precursor. PVP decomposition takes place between 350 °C to 450 °C,[46] which contributes to the most dramatic weight loss in the plot. Herein, merging of **i** and **ii** is observed because of the identical amount of PVP in both cases. Further slow

weight losing is detected in the range of 600 °C ~ 800 °C, which could be due to the transformation from α-Fe_2O_3 to FeO or Fe metal in N_2 atmosphere. The differential scanning calorimetry (DSC) data is also recorded, shown as curve **iii** and **iv** in Fig. 5**a**, which corresponds well with the TGA behaviour. At the two temperature ranges with dramatic weight loss (below 100°C and 350 °C ~ 450 °C), downward peaks are observed because additional heat is required to evaporate solvents and small molecules generated from materials decomposition.

The N_2 adsorption and desorption isotherm of La-doped hematite nanotubes depicts a large range of Ps/Po, matching with characteristics of a typical H3-type hysteresis loop (Fig. 5**b**). Such loop indicates the presence of slit-like macropores in the material, which is consistent with the FESEM image shown in Fig. 1**b**. BET surface area of the La-doped hematite nanotubes is measured to be 32.0 m^2/g, which is 45% larger than pristine hematite nanofibers.[47] Park and co-workers[48] also observed a similar surface area increase in their report of a template-based conversion from hematite nanorods to nanotubes.

FESEM EDX is performed to determine the element percentages as well as each element distribution in the La-doped hematite nanotubes. As shown in Fig. 6, the EDX spectrum shows sharp and strong peaks for Fe, O and La with atomic percentages of 30.47 mol%, 65.87 mol% and 3.66 mol%, respectively, which corresponds to a chemical formula of $La_{0.22}Fe_{1.78}O_3$. There are some extra O elements in the material, which is possibly due to oxygen-containing impurities. The extra unlabeled peaks in the spectrum are attributed to the coated gold or carbon substrate. From the mapping plot (Fig. 6 inset), it is observed that the La distribution aligns well with the FESEM image. Stronger La signals come from the central part of the plot where nanotubes are more densely packed. But the uneven distribution is not seen for Fe and O because their signals are too strong to differentiate the uneven material distribution.

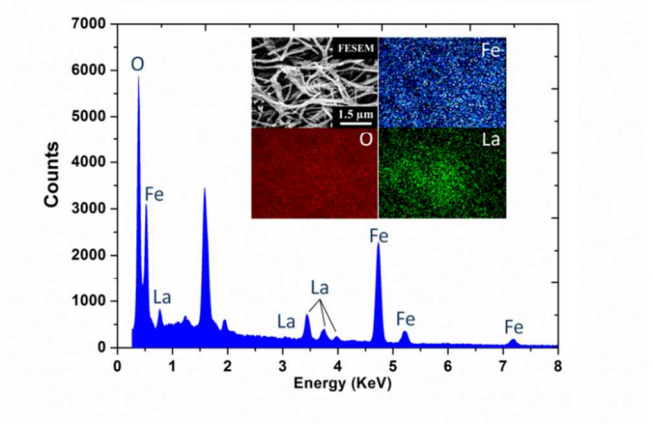

Fig. 6 EDX spectrum of La-doped hematite nanotubes with strong peaks for Fe, O and La. The unlabelled peaks results from the Au coating or carbon tape substrate. Inset is the element mapping for Fe, O and La.

Electrochemical Impedance Spectroscopy

To study the electrochemical properties of La-doped hematite, electrochemical impedance spectroscopy (EIS) investigation is performed under dark and light conditions with 1.23 V external bias vs RHE (see Fig. 7). This figure clearly shows that the La-doped hematite nanoparticles and nanotubes display much smaller semi-circle compared to the pristine nanoparticles and nanofibers under irradiation or dark conditions. This reveals the significant effect of La-doping on reducing charge transfer resistance at the hematite/electrolyte interface. Moreover, electrical conductivity characterization using four-probe system reveals that, conductivity of La-doped hematite is 151% higher than that of pristine counterpart, as shown in the inset of Fig. 7. These positive effects can be interpreted by the atom size and electronic structures of La dopant. La^{3+} ion possesses a much larger ion radius than Fe^{3+}, which makes it much easier for La^{3+} to contribute its outer shell electrons to the conductive carrier path in hematite. In principle, nanoparticles have higher packing density (see Fig. S1 and S2), therefore display less charge transfer resistances compared to nanotube or nanofibre counterparts. Accordingly in Fig. 7, we observed that, La-doped hematite nanoparticles (curve **h**) demonstrate less charge transfer resistance than nanotubes (curve **g**). Charge transfer resistance of pristine hematite nanoparticle (curve **f**) is also smaller than that of pristine nanofibers (curve **e**). This is in good agreement with the higher current density of nanoparticles relative to nanotubes (or nanofibers) shown in Fig. 8 and Fig. 9.

For all the nanostructures in Fig.7, the charge transfer resistance is higher under dark condition (curve **a**, **b**, **c** and **d**) than under light condition (curve **e**, **f**, **g** and **h**). This is because of the insulating nature of hematite in PEC test.[44] Upon light irradiation, the charge transfer resistance is reduced mainly due to the emerging of photogenerated charge carriers.

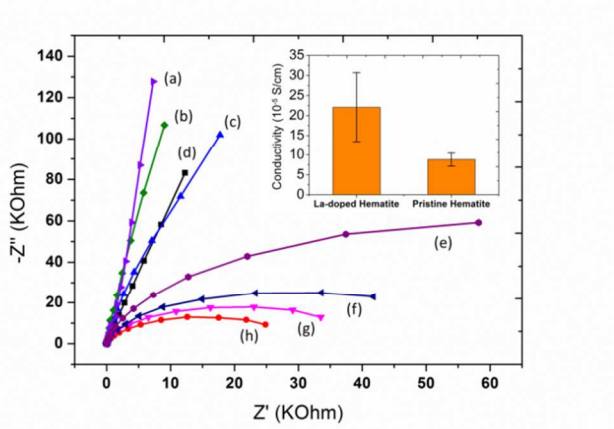

Fig. 7 Nyquist plot for pristine and La-doped hematite nanomaterial-based photoelectrode. Pristine nanofibers under (a) dark and (e) light conditions. Pristine nanoparticles under (b) dark and (f) light conditions. La-doped nanotubes under (c) dark and (g) light conditions. La-doped nanoparticles under (d) dark and (h) light conditions. Inset is result of conductivity measurement from four-probe system.

PEC Water Splitting Studies on La-doped Hematite

PEC water splitting studies is carried out using custom-made three electrode PEC cell in both dark and 100 mW/cm^2 simulated light irradiation conditions. The measured potentials versus Ag/AgCl (3M KCl) are converted to those versus reversible hydrogen electrode (RHE) using the Nernst Equation.[20] Fig. 8 shows the J-V curves of both La-doped and pristine hematite photoelectrodes under dark and simulated light irradiation conditions. Without La-doping, pristine hematite nanoparticles and nanofibers demonstrate similar but relatively low current densities (Fig. 8 **e** and **f, g** and **h**), mainly because pristine hematite acts as insulator when used as photoelectrode in PEC cell.[44] After La-doping, both the nanoparticles and nanotubes show improved current densities

(Fig. 8 **a** and **b, c** and **d**). According to the PEC results of La-doped hematite with different amounts of La-precursors, the sample prepared with 60 mg $La(acac)_3 \cdot xH_2O$ demonstrates the best photocurrent density. Thus 60 mg $La(acac)_3 \cdot xH_2O$ is chosen to prepare La-doped hematite in this study for material characterization and PEC measurement. The dark current densities at higher applied voltages (i.e. 1.60 V) increase significantly after La-doping, which is very likely due to the reduced charge transfer resistance and improved electrical conductivity. At light irradiation conditions, La-doping promotes the current density to 0.091 mA/cm^2 and 0.116 mA/cm^2 for nanotubes and nanoparticles at 1.23 V *vs.* RHE, corresponding to 60% and 183% increase compared to the pristine nanofibers and nanoparticles, respectively. At a relatively higher external bias of 1.60 V vs RHE, the positive effect of La-doping on PEC performance is also significant. The results show that, at 1.60 V vs RHE, Tthe current densities of La-doped hematite nanotubes and nanoparticles further increase to 0.329 mA/cm^2 and 0.509 mA/cm^2, which are 98 % and 169% higher compared to the pristine nanofibers and nanoparticles, respectively.

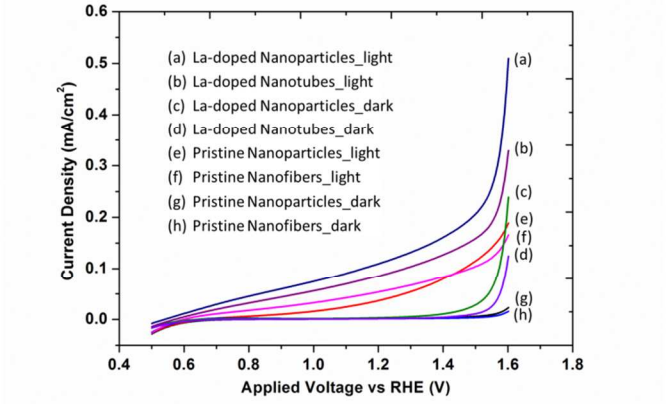

Fig. 8 J-V curve measured for pristine and La-doped hematite photoelectrodes under dark and 100 mW/cm^2 simulated solar irradiation with a scan rate of 10 mV/s in 1 M KOH electrolyte.

For La-doped hematite nanostructures, it can be clearly observed that the nanoparticles display higher current density than nanotubes under irradiation or dark conditions (In Fig. 8: **a** vs **b**, **c** vs **d**). This is because the La-doped hematite has lower charge transfer resistance and higher electrical conductivity. Thus the positive effect of higher packing density of nanoparticles is significant enough to be tested against nanotubes. But for pristine hematite nanostructures, their charge transfer resistance is so large that the effect of higher packing density of nanoparticles becomes too small to be tested. Therefore, the pristine hematite nanoparticles display comparable current density with nanofibers under irradiation or dark conditions (In Fig. 8: **e** vs **f**, **g** vs **h**).

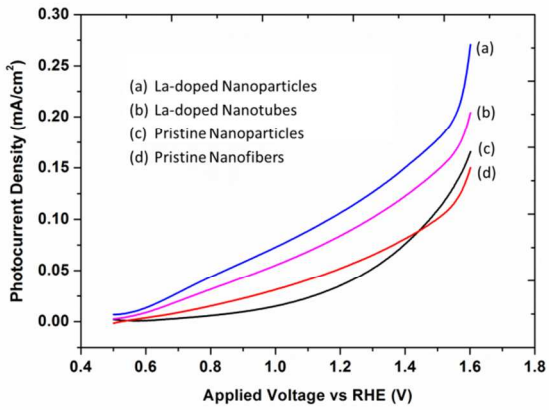

Fig. 9 Net photocurrent densities measured for pristine and La-doped hematite photoelectrodes by subtracting the dark current densities from the overall current density.

Fig. 9 depicts the net current densities induced by photoeffect for La-doped and pristine hematite photoelectrodes. It can be clearly seen that La-doping is able to improve the photo-response throughout the entire voltage window. And the improvement is more prominent at relatively lower applied voltages (i.e. 1.23 V) than the higher ones (i.e. 1.60 V). The data are summarized in Table 1. Besides the enhanced charge transportation properties aforementioned, such improvement could also be attributed to the narrowed bandgap width, which affords more efficient absorption of the incident photons. Furthermore, the oxygen content within electrolyte is determined using oxygen detector. Bare KOH electrolyte gives rise to an oxygen content of 69.9%, which increases to 73.4%, 82.0% and 81.8% after 20min, 40min and 60min PEC reaction respectively (see Fig. S3). While after left open to air overnight, all the samples demonstrate a notable drop of oxygen content. Therefore, oxygen evolution on the hematite photoelectrode is confirmed and the reaction is formulated as shown below.

$$2OH^- + 2h^+ \rightarrow H_2O + \frac{1}{2}O_2$$

Table 1 Net photocurrent densities of the prepared hematite photoelectrodes

	Sample	Photocurrent Density (mA/cm^2)		PEC Improvement
		Pristine	**Doped**	
1.23 V	Nanotubes (or fibers)*	*0.055*	*0.089*	*61%*
	Nanoparticles	*0.039*	*0.112*	*187%*
1.60 V	Nanotubes (or fibers)*	*0.150*	*0.204*	*36%*
	Nanoparticles	*0.166*	*0.270*	*63%*

* La-doped Hematite Nanotubes *vs* pristine Hematite Nanofibers.

Conclusions

We demonstrated electrospinning is a facile and practical method in doping La^{3+} cations into hematite nanotubes. HRTEM and XRD reveal that La-cations are doped into hematite crystal lattice and also expand the lattice spacing. EIS and electrical conductivity characterization studies reveal that doping a small amount (3.66 mol%) of La^{3+} can significantly reduce charge transfer resistance and increase electrical conductivity. Light absorption of hematite nanomaterial is also improved by the reduced bandgap width. In PEC water splitting studies, La-doped hematite nanoparticles demonstrate a net photocurrent density of 0.112 mA/cm^2 at 1.23 V vs RHE under 100 mW/cm^2 irradiation, which is 187% higher than pristine hematite nanoparticles. The La-doped hematite nanotubes also

demonstrate 61% higher net photocurrent density than pristine hematite nanofibers. The intensification of crystal orientation along (110) plane and lattice expansion caused by the La^{3+} cations are likely the two main factors that account for the positive effect of La-doping. We hope this study could inspire enhancing the electrical conductivity and PEC performance of hematite nanostructures by doping rare earth metals.

Acknowledgements

This work was supported by Institute of Materials Research and Engineering (IMRE), Agency for Science, Technology and Research (A*STAR) (Grant Code: IMRE/12-1C0101). Special thanks to Mr. Lim Poh Chong, Ms. Lai Mei Ying Doreen, Ms. Ni Xiping and Ms. Koh Xue Qi from IMRE for their invaluable assistance in XRD, FESEM EDX, BET and DSC analysis.

Notes

[a] Institute of Materials Research and Engineering, Agency for Science, Technology and Research, 3 Research Link, Singapore 117602.

[b] NUSNNI, National University of Singapore, 2 Engineering Drive 3, Singapore 117576.

[c] Environmental & Water Technology, Centre of Innovation, Ngee Ann Polytechnic, Singapore, 599489.

[d] Department of Biomedical Engineering, National University of Singapore, 9 Engineering Drive, Singapore 117576

[e] Department of Chemistry, National University of Singapore, 3 Science Drive 3, Singapore 117543.

* Corresponding Author: seeram@nus.edu.sg

** Corresponding Author: luoh@imre.a-star.edu.sg

References

1. D. A. Wheeler, G. Wang, Y. Ling, Y. Li and J. Z. Zhang, *Energy. Environ. Sci*., 2012, **5**, 6682.
2. J. J. Jiang, Y. Li, J. Liu, X. Huang, C. Yuan and X. W. Lou, *Adv. Mater.*, 2012, **24**, 5166.
3. M. Zhi, C. Xiang, J. Li, M. Li and N. Wu, *Nanoscale*, 2013, **5**, 72.
4. R. S. Devan, R. A. Patil, J.-H. Lin and Y.-R. Ma, *Adv. Funct. Mater*,. 2012, **22**, 3326.
5. K. Honda and A. Fujishima, *Nature*, 1972, **238**, 37.
6. T. J. Wong, F. J. Lim, M. Gao, G. H. Lee and G. W. Ho, *Catal. Sci. Technol.*, 2013, **3**, 1086.
7. J. Wang, M. Gao and G. W. Ho, *J. Mater. Chem. A*, 2014, **2**, 5703.
8. Y. Wang, J. Wu, J. Zheng, R. Jiang and R. Xu, *Catal. Sci. Technol.*, 2012, **2**, 581.
9. Y. Wang, Y. Wang and R. Xu, *Int. J. Hydro. Energy*, 2010, **35**, 5245.
10. J. Hong, Y. Wang, Y. Wang, W. Zhang and R. Xu, *ChemSusChem*, 2013, **6**, 2263.
11. D. R. Whang, K. Sakai and S. Y. Park, *Angew. Chem. Int. Ed.*, 2013, **52**, 11612.
12. C. V. Suneesh, B. Balan, H. Ozawa, Y. Nakamura, T. Katayama, M. Muramatsu, Y. Nagasawa, H. Miyasaka and K. Sakai, *Phys. Chem. Chem. Phys.*, 2014, **16**, 1607.
13. S. M. Ahmed, J. Leduc and S. F. Haller, *J. Phys. Chem.*, 1988, **92**, 6655.
14. A. B. Murphy, P. R. F. Barnes, L. K. Randeniya, I. C. Plumb, I. E. Grey, M. D. Horne and J. A. Glasscock, *Int. J. Hydro. Energy*, 2006, **31**, 1999.
15. J. C. Launay, *Journal of Crystal Growth*, 1982, **57**, 118.
16. J. H. Kennedy and K. W. Frese, Jr, *Journal of Electrochemical Society*, 1978, **125**, 709.
17. I. Cesar, K. Sivula, A. Kay, R. Zboril and M. Grätzel*, J. Phys. Chem. C.*, 2009, **113**, 772.
18. M. P. Dare-Edwards, J. B. Goodenough, A. Hamnett and P. R. Trevellick, *J. Chem. Soc., Faraday Trans. 1*, 1983, **79**, 2027.
19. I. Cesar, A. Kay, J. A. G. Martinez and M. Grätzel, *J. Am. Chem. Soc.*, 2006, **128**, 4582.
20. Y. Ling, G. Wang, D. A. Wheeler, J. Z. Zhang and Y. Li, *Nano Lett.*, 2011, **11**, 2119.
21. P. Zhang, A. Kleiman-Shwarsctein, Y.-S. Hu, J. Lefton, S. Sharma, A. J. Forman and E. McFarland, *Energy Environ. Sci.*, 2011, **4**, 1020.
22. C. J. Sartoretti, B. D. Alexander, R. Solarska, I. A. Rutkowska, J. Augustynski and R. Cerny, *J. Phys. Chem. B*, 2005, **109**, 13685.
23. W. B. Ingler Jr and S. U. M. Khan, *Thin Solid Films*, 2004, **461**, 301.
24. V. R. Satsangi, S. Kumari, A. P. Singh, R. Shrivastav and S. Dass, *Inter. J. Hydro. Energy*, 2008, **33**, 312.
25. S. U. M. Khan and Z. Y. Zhou, *J. Electroanal. Chem*., 1993, **357**, 407.
26. A. Kleiman-Shwarsctein, Y.-S. Hu, A. J. Forman, G. D. Stucky and E. W. McFarland, *J. Phys. Chem. C*, 2008, **112**, 15900.
27. K. Sivula, R. Zboril, F. L. Formal, R. Robert, A. Weidenkaff, J. Tucek, J. Frydrych and M. Grätzel, *J. Am. Chem. Soc.*, 2010, **132**, 7436.
28. M. Zhang, W. Luo, Z. Li, T. Yu and Z. Zou, *Applied Physics Letters*, 2010, **97**, 042105.
29. L. Vayssieres, N. Beermann, S.-E. Lindquist and A. Hagfeldt, *Chemistry of Materials*, 2001, **13**, 233.
30. S. D. Tilley, M. Cornuz, K. Sivula and M. Grätzel, *Angew. Chem. Int. Ed.*, 2010, **49**, 6405.
31. A. Mao, G. Y. Han and J. H. Park, *J. Mater. Chem.*, 2010, **20**, 2247.
32. S. Cavaliere, S. Subianto, I. Savych, D. J. Jones and J. Rozière, *Energy Environ. Sci.*, 2011, **4**, 4761.
33. V. Thavasi, G. Singh and S. Ramakrishna, *Energy Environ. Sci.*, 2008, **1**, 205.
34. G. Wang, P. Wang, H.-K. Luo and T. S. A. Hor, *Chem. Asian J.*, 2014, DOI: 10.1002/asia.201402007.
35. T. Suzuki, T. Hisatomi, K. Teramura, Y. Shimodaira, H. Kobayashi and K. Domen, *Phys. Chem. Chem. Phys.*, 2012, **14**, 15475.
36. S. L. Liew, Z. Zhang, T. W. G. Goh, G. S. Subramanian, H. L. D. Seng, T. S. A. Hor, H. -K. Luo and D. Z. Chi, *Inter. J. Hydro. Energy*, 2014, **39**, 4291.
37. K. Gömann, G. Borchardt, M. Schulz, A. Gömann, W. Maus-Friedriches, B. Lesage, O. Kaïtasov, S. Hoffmann-Eifert and T. Schneller, *Phys. Chem. Chem. Phys.*, 2005, **7**, 2053.
38. S. N. Tijare, M. V. Joshi, P. S. Padole, P. A. Mangrulkar, S. S. Rayalu and N. K. Labhsetwar, *Inter. J. Hydro. Energy*, 2012, **37**, 10451.
39. M. Zhang, Y. Lin, T. J. Mullen, W.-f. Lin, L.-D. Sun, C.-H. Yan, T. E. Patten, D. Wang and G.-y. Liu, *J. Phys. Chem. Lett*., 2012, **3**, 3188.

40. Y. Cheng, B. Zou, C. Wang, Y. Liu, X. Fan, L. Zhu, Y. Wang, H. Ma and X. Cao, *CrystEngComm*, 2011, **13**, 2863.
41. C. T. Cherian, J. Sundaramurthy, M. Kalaivani, P. Ragupathy, P. S. Kumar, V. Thavasi, M. V. Reddy, C. H. Sow, S. G. Mhaisalkar and S. Ramakrishna, B. V. R. Chowdari, *J. Mater. Chem.*, 2012, **22**, 12198.
42. R. Liu, C. Zhang and J. Ma, *Journal of Rare Earths*, 2010, **28**, 376.
43. N. Iordanova, M. Dupuis and K. M. Rosso, *J. Chem. Phys.*, 2005, **122**, 144305.
44. A. Kay, I. Cesar and M. Grätzel, *J. Am. Chem. Soc.*, 2006, **128**, 15714.
45. B. Pal and M. Sharon, *Thin Solid Films*, 2000, **379**, 83.
46. Y. K. Du, P. Yang, Z. G. Mou, N. P. Hua and L. Jiang, *Journal of Applied Polymer Science*, 2006, **99**, 23.
47. J. Sundaramurthy, P. S. Kumar, M. Kalaivani, V. Thavasi, S. G. Mhaisalkar and S. Ramakrishna, *RSC Advances*, 2012, **2**, 8201.
48. A. Mao, K. Shin, J. K. Kim, D. H. Wang, G. Y. Han and J. H. Park, *ACS Appl. Mater. Interfaces*, 2011, **3**, 1852.